SPIN90 modulates the architecture of lamellipodial actin in an ARPC5L dependent fashion.

LuYan Cao[1,2*], Angika Basant[1†], Miroslav Mladenov[1], Naoko Kogata[1], Antoine Jegou[2], Guillaume Romet-Lemonne[2], Sophie Brasselet[3], Manos Mavrakis[3], Michael Way[1,4*]

1. The Francis Crick Institute, 1 Midland Road, London, NW1 1AT, UK.
2. Université Paris Cité, CNRS, Institut Jacques Monod, 75013 Paris, France.
3. Institut Fresnel, CNRS UMR7249, Aix Marseille Univ, Centrale Med, 13013 Marseille, France
4. Department of Infectious Disease, Imperial College, London W2 1PG, UK.

[†] Current address: King's College London, Guy's Campus, London, SE1 1UL, UK

* Joint corresponding authors: luyan.cao@ijm.fr; michael.way@crick.ac.uk

Abstract

When stimulated by nucleation-promoting factors such as WAVE, the Arp2/3 complex generates branched actin networks. In contrast, when activated by SPIN90, the Arp2/3 complex generates linear actin filaments. The Arp2/3 complex in mammals, consists of 8 iso-complexes with different properties as there are two isoforms of Arp3, ArpC1 and ArpC5. Here, using recombinant Arp2/3 iso-complexes with defined composition, we show that SPIN90 selectively activates ArpC5L rather than ArpC5 containing complexes to generate linear actin filaments. Consistent with this, SPIN90 at the leading edge of migrating cells enhances the recruitment of ArpC5L but not ArpC5 containing Arp2/3 complexes to lamellipodia. These SPIN90-Arp2/3-ArpC5L complexes generate linear actin filaments that integrate into lamellipodia and impact protrusion efficiency. Moreover, loss of SPIN90 leads to an enrichment in actin filaments that are more perpendicular to the plasma membrane. Our results demonstrate that SPIN90 regulates the architecture and dynamics of lamellipodial actin in an Arp2/3 iso-complex dependent fashion.

Teaser

SPIN90 selectively recruits and activates ArpC5L containing Arp2/3 to shape the architecture and dynamics of lamellipodial actin.

Introduction

Highly conserved throughout evolution, the Arp2/3 complex is a unique actin nucleator, essential for generating branched actin networks (*1-4*). Consequently, the Arp2/3 complex is an important regulator of the architecture and dynamics of the actin cytoskeleton (*5-9*). Activated by class I nucleation-promoting factors (NPFs), such as WAVE, N-WASP, WASP, and WASH, the Arp2/3 complex can bind to pre-existing actin filaments, also known as mother filaments, and initiate the formation of a new actin branch, or a daughter filament (*9-11*). Alternatively, when activated by SPIN90 (also known as WISH, NCKIPSD, or Dip1), the Arp2/3 complex is unable to bind to an existing actin filament and rather generates a new linear actin filament (*8, 12*). Given its ability to nucleate actin networks, the Arp2/3 complex is indispensable for various cellular functions, including endocytosis, cell migration, cortical actin regulation and DNA repair (*2, 13-17*).

The Arp2/3 complex contains seven subunits, the Actin Related Proteins Arp2 and Arp3, as well as ArpC1-ArpC5 (*1, 3, 18*). In higher eukaryotes, such as mammals, there are two isoforms of Arp3, ArpC1, and ArpC5, encoded by distinct genes (*1, 19, 20*). In humans, Arp3 and Arp3B are 91% identical, while ArpC1A/ArpC1B and ArpC5/ArpC5L each share 67% identity (*21*). These different subunit isoforms have been shown to give the Arp2/3 complex distinct cellular and physiological functions (*11, 22-24*). In addition, mutations in human ArpC1B cause severe inflammation and immunodeficiency (*25, 26*). Loss of ArpC5 also leads to multiple congenital deficiencies, inflammation, dysregulated host-microbiome interactions, and increased mortality (*27-29*).

To understand the molecular mechanism underlying these phenotypes, it is essential to dissect the properties of the different Arp2/3 iso-complexes. Arp2/3 iso-complexes have subtly but recognizably different structural conformations (*24, 30, 31*) and respond differently to the widely used Arp2/3 inhibitors, CK-666 and CK-869 (*32*). Previous studies have also shown that all Arp2/3 iso-complexes, regardless of their subunit composition, can generate actin branches. Complexes containing ArpC1B or ArpC5L are, however, more efficient at branch formation than those with ArpC1A or ArpC5 (*21*), while networks generated by Arp3B-containing complexes disassemble faster than those formed by Arp3-containing complexes in cells due to oxidation of Methionine 293 of Arp3B by MICAL2 (*33*).

In contrast, it is still unclear whether all Arp2/3 iso-complexes generate linear actin filaments when activated by SPIN90. In particular, our previous work demonstrated that although CK-666 inhibits all Arp2/3 iso-complexes from generating linear filaments, it only blocks ArpC1A containing complexes producing actin branches (*32*). These findings suggest that different Arp2/3 iso-complexes engage fundamentally distinct mechanisms depending on whether activation drives linear filament formation or actin branching.

In this study, using in vitro biochemical approaches, we found that only the ArpC5L-containing Arp2/3 complex can generate linear actin filaments. Moreover, SPIN90

accumulates at the leading edge of lamellipodia, where it recruits and activates ArpC5L-, but not ArpC5-containing Arp2/3 complexes. These linear filaments nucleated by SPIN90-Arp2/3-ArpC5L complexes shape the architecture of lamellipodial actin, impacting actin dynamics and leading-edge protrusion.

Results

Spin90 activates ArpC5L- but not the ArpC5-containing Arp2/3 complexes.

Using purified recombinant human Arp2/3 iso-complexes with defined compositions, we performed pyrene actin polymerisation assays to examine their capacity to accelerate actin polymerisation when activated by SPIN90. We found that, in the presence of SPIN90, Arp2/3 complexes containing ArpC1A-ArpC5L or ArpC1B-ArpC5L significantly increase the rate of actin polymerization compared to controls lacking SPIN90 (Fig. 1A). In contrast, Arp2/3 complexes containing ArpC1A-ArpC5 or ArpC1B-ArpC5 only induced actin polymerisation at levels slightly above controls when activated by SPIN90. These differences suggest SPIN90 only efficiently activates Arp2/3 complexes containing ArpC5L to generate linear filaments.

To further confirm this, we performed TIRF microscopy to directly observe the generation of linear actin filaments by the different Arp2/3 iso-complexes in the presence of SPIN90. Actin alone, or in combination with Arp2/3 complexes, does not efficiently nucleate filament formation (Fig. 1B). When incubated with SPIN90, Arp2/3 complexes containing ArpC5, whether paired with ArpC1A or ArpC1B, had an extremely limited increase in actin nucleation. In contrast, Arp2/3 complexes containing ArpC5L, regardless of the ArpC1 isoform, produce linear filaments with 20- to 40-fold greater efficiency in the presence of SPIN90 (Fig. 1B). These results clearly show that linear actin filaments are generated by SPIN90-activated ArpC5L-containing Arp2/3 complexes.

SPIN90 has a higher affinity for Arp2/3 complexes containing ArpC5L

Our findings that only ArpC5L-containing complexes can be efficiently activated by SPIN90 raises the question: what is the molecular basis for the differing efficiencies of linear filament nucleation among Arp2/3 iso-complexes? The recent structure of SPIN90 in complex with Arp2/3 reveals it binds directly to the ArpC5/ArpC5L subunit, as well as to Arp2, Arp3, ArpC2 and ArpC4 (Fig. 2A, S1A) (*12, 34, 35*). Given our observations, we wondered whether the ArpC5 subunit incorporation determines the affinity between SPIN90 and the Arp2/3 complex. To investigate this, we examined the affinity between Arp2/3 iso-complexes and SPIN90 using GST pull-down assays. We found that GST-SPIN90 pulled down more Arp2/3 complexes containing ArpC5L compared to those with ArpC5, regardless of the ArpC1 subunit isoform (Fig. S1B).

To quantify the affinity of SPIN90 for Arp2/3 complexes containing either ArpC5L or ArpC5, we performed GST pull-down assays on Arp2/3 complexes containing ArpC1B/ArpC5 or ArpC1B/ArpC5L. As recent work has shown that SPIN90 forms a homodimer that simultaneously binds two Arp2/3 complexes (*34, 35*), we used the Hill equation to fit the experimental data and examine whether the Arp2/3 complex binds to SPIN90 in a cooperative manner (Fig. 2B, C, S1C). The fitting revealed that SPIN90 binds the ArpC1B/ArpC5L-containing Arp2/3 complex with a dissociation constant (K_D) of 3.01 ± 0.85 µM and a Hill coefficient of 1.59 ± 0.67, suggesting the possible presence of positive cooperativity. In contrast, the low amount of ArpC5-containing complex pulled down with GST-SPIN90 prevented reliable fitting so a dissociation constant (K_D) could not be determined. These results confirmed that the ArpC5 subunit isoforms have a strong impact on the affinity of SPIN90 for Arp2/3 iso-complexes. Furthermore, it provides an explanation why, SPIN90 effectively only activates ArpC5L-containing Arp2/3 complexes to generate linear actin filaments in our in vitro experiments.

SPIN90 co-localizes with Arp2/3 complex at the leading edge

Another key question is the physiological impact of the selective interaction between SPIN90 and Arp2/3–ArpC5L in cells. To study the impact of SPIN90 and Arp2/3 on the cellular actin, we used B16 cells which have large and constant lamellipodial branched actin networks (*36, 37*). We began by assessing the expression level of ArpC5 and ArpC5L containing Arp2/3 complexes in B16 cells through quantitative immunoblot analysis, using recombinant mouse ArpC5 and ArpC5L subunits as standards (Fig. 3A). We found that ArpC5 and ArpC5L are both expressed in B16 cells, with ArpC5L levels being ~1.7-fold higher than ArpC5.

Then, we investigated the localisation of SPIN90 in B16 cells. We tested several SPIN90 antibodies, including commercial and homemade ones, but none worked on mouse cell lines for immunofluorescence analysis. We therefore expressed Ruby-tagged SPIN90 to visualize the localization of SPIN90 in live cells. We found that Ruby-SPIN90 is predominantly cytoplasmic, but the protein is enriched at the leading edge of lamellipodia which is not observed with the GFP internal control (Fig. 3B, Movie S1). A similar accumulation at the leading edge was observed for a Ruby-SPIN90 Nter construct that lacks the Arp2/3 interacting C-terminal Leucine Rich Region (LRR) of SPIN90 (Fig. 3B, Movie S2). This localisation demonstrates that the N-terminus of SPIN90 responds to an upstream signal responsible for determining the localisation of SPIN90.

Both SPIN90 and Arp2/3 integrate into lamellipodial actin

To visualize both ArpC5L and SPIN90 at the same time we expressed Ruby-SPIN90 in B16 cell lines in which NeonGreen is linked to the N-terminus of ArpC5L at its endogenous gene locus (Fig. S2A). Although we cannot distinguish ArpC5L bound to SPIN90 from ArpC5L located at actin branches, we observed that both ArpC5L and

SPIN90 accumulate at the leading edge of lamellipodia. Interestingly, during live imaging, we observed that both proteins initially appear at the leading edge and then move rearward toward the cell body before disappearing (Movie S3). Hence, the trajectories of NeonGreen-ArpC5L and Ruby-SPIN90-FL display similar patterns, characterized by straight lines perpendicular to the leading edge (Fig. 4A). Although the rearward flow of Arp2/3 complexes has been described (*36*), this is the first time such retrograde flow of SPIN90 has been seen in lamellipodia (Fig. 4A).

To determine whether SPIN90 integrates into the actin network through its interaction with the Arp2/3 complex, we examined the behaviour of Ruby-SPIN90 Nter in B16 cells expressing endogenous NeonGreen-ArpC5L. Live cell imaging reveals that while NeonGreen-ArpC5L undergoes retrograde flow, Ruby-SPIN90 Nter remained at the leading edge and did not move inward toward the cell body (Movie S4). The trajectories of NeonGreen-ArpC5L and Ruby-SPIN90 Nter exhibit distinct patterns (Fig. 4A).

To analyse trajectories of SPIN90 and ArpC5L in more detail, we generated kymographs, which revealed that both proteins move at similar velocities (Fig. 4B). Taken together, our observations indicate that SPIN90, through its binding to Arp2/3 complexes, integrates into lamellipodial networks and undergoes retrograde flow.

SPIN90 enhances ArpC5L but not ArpC5 recruitment to the leading edge

Our in vitro data demonstrate that SPIN90 interacts much better with Arp2/3 complexes containing ArpC5L, than those with ArpC5. To examine if SPIN90 enhances the recruitment of ArpC5L-containing Arp2/3 complexes, we quantified the level of NeonGreen-ArpC5L at the leading edge in the presence and absence of SPIN90 (Fig. 5A). We observed that in SPIN90 depleted cells (Fig. S2), the NeonGreen-ArpC5L signal at the leading edge is reduced compared to control cells. When ArpC5 is knocked down, we observed increased recruitment of NeonGreen-ArpC5L to the leading edge, to compensate for the absence of ArpC5-containing complexes. Importantly, the depletion of SPIN90 in the absence of ArpC5 still results in reduced recruitment of ArpC5L to the leading edge (Fig. 5A). Meanwhile, our Western blots confirmed that SPIN90 depletion does not affect the expression of ArpC5 isoforms, in addition the depletion of ArpC5 or ArpC5L has little impact on the expression of the other isoforms (Fig. S2).

In contrast to ArpC5L, the signal of endogenous NeonGreen tagged ArpC5 at the leading edge does not negatively correlate with the depletion of SPIN90 as it increases (Fig. 5B). These observations support the hypothesis that SPIN90 enhances the recruitment of ArpC5L, but not ArpC5, to the leading edge.

SPIN90 regulates lamellipodial actin architecture via ArpC5L

Arp2/3-mediated branches are geometrically constrained to form at an angle of approximately 70 degrees (*7*). However, it has been reported that Arp2/3 complexes containing either ArpC5 or ArpC5L have a distinct impact on the architecture of lamellipodial actin networks although the mechanistic basis for this difference has not been established (*24*). Given that SPIN90 generates linear filaments only with ArpC5L-containing complexes, we wondered what impact its presence has on the architecture of lamellipodial actin networks.

Using polarized fluorescence microscopy (*38*), we quantified the organization of actin filaments in lamellipodia, excluding microspikes, in Alexa-488 phalloidin-stained cells. The Alexa-488 conjugate in phalloidin is constrained in mobility and is parallel to the axis of the actin filament helix (*38*). Thus, the orientation of Alexa-488 is a direct readout of actin filament mean orientation (angle rho, ρ) within a scale of ~200nm (i.e. the optical resolution limit, Fig. 6A, B). Its angular spread around the mean orientation at each pixel is a complementary readout of actin filament alignment (angle psi, ψ) at the molecular level, within the scale of ~200 nm (Fig. 6A, S3A-C).

We measured high ψ values for lamellipodial actin (mean = 157°) in wildtype cells, as well as in all KO cell lines (Fig. S3A-C), with no detectable statistical difference among the different cell lines. This finding is in line with electron microscopy showing that lamellipodial actin filaments explore varying orientations within the scale of ~200 nm (Fig. 6A, B), and with quantification of branch densities which were comparable in tomograms of WT, ArpC5 KO and ArpC5L KO cell lines (*24*).

Importantly, quantification of mean actin filament orientations showed distinct differences among the different cell lines (Fig. 6A-F and Fig. S3D). Whereas lamellipodial actin in WT cells enriches in populations more perpendicular to the leading edge, the distribution of filament orientations, both per pixel (Fig. 6C, D and Fig. S3D) and averaged per lamellipodium (Fig. 6E, F), is much broader in ArpC5 KO cells. This increased variability, reflected by the higher standard deviation (SD) of the respective distribution, indicates the coexistence of filament populations more parallel to the leading edge. These observations are consistent with the quantification of filament angles obtained from cryo-electron tomograms of WT and ArpC5 KO cells (*24*). Importantly, lamellipodial actin filaments in both ArpC5L KO and SPIN90 KO cells not only remained enriched in populations more perpendicular to the leading edge, but the respective distributions, both per pixel (Fig. 6B-D and Fig. S3D) and averaged per lamellipodium (Fig. 6E, F), were also narrower than in WT cells. It reflects the presence of a larger population of filaments with angles perpendicular to the leading edge. This finding is fully consistent with the quantification of filament angles from cryo-electron tomograms in ArpC5L KO cells (*24*), and further corroborates that SPIN90 regulates lamellipodial actin architecture via ArpC5L.

Arp2/3-mediated branches follow a characteristic average 70-degree geometry whereas SPIN90–Arp2/3-nucleated linear actin filaments can in principle orient in all directions. We therefore hypothesized that the absence of this linear filament population is responsible for the enrichment of filaments with angles perpendicular to the leading edge in both ArpC5L KO and SPIN90 KO cells. Moreover, this predicts a broader distribution of filament angles in cells overexpressing SPIN90. Consistent with this, we found that cells expressing Ruby-SPIN90 had a wider distribution of filament angles than those expressing Ruby-SPIN90 Nter which cannot interact with the Arp2/3 complex, the latter being comparable to wildtype cells (Fig. 6G, H and Fig. S3E, F).

SPIN90 regulates lamellipodial protrusion

To examine the impact of the SPIN90 interaction with ArpC5L-containing Arp2/3 complexes on lamellipodial protrusion, we generated B16 cells with endogenously tagged GFP-β-actin and lacking either the ArpC5 isoforms or SPIN90 respectively (Fig. 7A, S4A). As previously reported by Fässler et al. (2023), we observed that in B16 cells the absence of ArpC5 reduces lamellipodial width, while the loss of ArpC5L increases it (Fig. 7B). The SPIN90 KO cells have lamellipodia of similar width to those of wild-type cells (Fig. 7B). Quantification of the lamellipodial actin density (GFP-β-actin intensity) revealed that the actin density decreased in ArpC5 KO cells compared to wild type controls. In contrast, lamellipodial actin density increased in the ArpC5L and SPIN90 KO cells compared to controls (Fig. 7B).

We performed FRAP analysis and quantified the protrusion rate and rearward flow of lamellipodial actin (Fig. 7C). Our results confirmed that the loss of ArpC5 reduces the lamellipodial protrusion rate, while the absence of ArpC5L does not have a strong impact on protrusion. Nevertheless, we found that SPIN90 KO cells consistently exhibit a slower protrusion rate compared to controls (Fig. 7D). We did not observe any significant difference in rearward flow between the wild-type and the three KO cell lines. The sum of rearward flow and protrusion rate was considered the lamellipodial actin polymerization rate (Fig. S4B). When we calculated protrusion efficiency by dividing the protrusion rate by the actin polymerization rate, we found that ArpC5L KO cells maintain a protrusion efficiency comparable to wildtype cells, whereas both ArpC5 KO and SPIN90 KO cells have reduced protrusion efficiency (Fig. 7D). Consistent with this, in a random migration assay using unlabelled B16 cells, we observed that ArpC5 KO and SPIN90 KO cells migrated more slowly compared with wild-type and ArpC5L KO cells (Fig. 7E). Although the p-values did not reach statistical significance ($p = 0.15$ for WT vs. ArpC5 KO; $p = 0.13$ for WT vs. SPIN90 KO), the effect sizes were large (Cohen's $d = 1.7$ for WT vs. ArpC5 KO; Cohen's $d = 1.9$ for WT vs. SPIN90 KO), suggesting potentially meaningful differences that may warrant further investigation with a larger sample size.

We hypothesized that SPIN90–Arp2/3–nucleated linear actin filaments help support lamellipodial protrusion. To test this notion, we overexpressed Ruby-SPIN90 in B16 cells and found as predicted that Ruby-SPIN90 increased the lamellipodial protrusion rate (Fig. 7F).

Discussion

Using in vitro biochemical approaches, we have now shown that the initiation of linear actin filaments by Arp2/3 complexes is determined by the composition of their ArpC5 subunits. Only Arp2/3 complexes containing ArpC5L and not those with ArpC5, can be efficiently activated by SPIN90 (Fig. 1, 8A), due to their differing affinity for this nucleation promoting factor (Fig. 2). This makes SPIN90 the first Arp2/3 activator with a clear preference for a subset of Arp2/3 iso-complexes with a defined composition. Our findings strengthen the hypothesis that Arp2/3 iso-complexes have distinct molecular and cellular properties determined by their subunit composition.

We also found that SPIN90 accumulates at the leading edge of lamellipodia (Fig. 3B) where it enhances the recruitment of ArpC5L- but not ArpC5-containing Arp2/3 iso-complexes (Fig. 5, 8A). Importantly, we also observed the rearward flow of both ArpC5L and SPIN90 (Fig. 4). Retrograde lamellipodial actin flow is known to result from myosin contraction and the resistive forces encountered during protrusion (*39, 40*). It is also established that after initiating a branch, the Arp2/3 complex remains at the branching point and becomes integrated into the branched actin network (*36*). The fact that SPIN90, but not its N-terminal domain which cannot bind Arp2/3, undergoes rearward flow indicates that SPIN90 and Arp2/3 integrate into lamellipodial actin together, presumably through crosslinking between SPIN90-Arp2/3-nucleated linear filaments and the rest of the lamellipodial actin.

Furthermore, using polarized fluorescence microscopy (*38*), we found that both SPIN90 and ArpC5L contribute to the enrichment of actin filaments with angles more parallel to the leading edge, whereas those formed by ArpC5 are more perpendicular (Fig. 6A-F). This is likely because branches generated by Arp2/3 are constrained by two factors: the orientation of pre-existing mother filaments and the fixed 70° branching angle dictated by the Arp2/3 complex structure. In contrast, linear filaments generated by SPIN90–Arp2/3–ArpC5L are likely more free to orient in any direction before being crosslinked to actin filaments in the lamellipodia (Fig. 8). The presence of SPIN90 and ArpC5L-containing complexes therefore increases the diversity of filament orientations at the leading edge.

Our observations of ArpC5 KO and ArpC5L KO lamellipodial actin networks using polarized fluorescence microscopy are fully consistent with previous reports based on high-resolution electron microscopy (*24*). Importantly, they further corroborate that SPIN90 works together with ArpC5L to regulate lamellipodial actin architecture. Although, compared with EM, we lack information on the orientation of individual actin filaments, our approach provides accurate measurements of the mean orientation and alignment of actin filaments at the molecular scale across a large

number of cells, as well as in much larger areas. This approach also offers the possibility of studying actin architecture through live imaging (*38*), thereby enabling simultaneous observation of cell behaviour and actin organization in the future.

Finally, we show that depletion of SPIN90 downregulates both the lamellipodial protrusion rate and cell motility speed (Fig. 7D, E). We believe that actin dynamics and architecture — including both filament orientation angles and their distribution — must be finely tuned to ensure efficient lamellipodial protrusion and cell migration. Accordingly, SPIN90 KO cells, which exhibit a narrower distribution of filament orientations, display reduced protrusion efficiency. In contrast, despite having a similar lamellipodial architecture, ArpC5L KO cells maintain a protrusion rate comparable to that of wild-type cells. This may be attributed to the positive correlation between ArpC5-nucleated branches and Ena/VASP activity, which promotes rapid actin filament elongation (*24*). Moreover, the low protrusion speed and motility observed in ArpC5 KO cells are likely the result of a combination of their negative correlation with Ena/VASP and an actin architecture, in which too many filaments are oriented toward the leading edge at shallow angles. Here we illustrate the importance of actin architecture on the lamellipodia protrusion efficiency. Nevertheless, a systematic understanding of how actin architecture and dynamics impact protrusion efficiency, particularly under different mechanical external conditions remains to be established.

Acknowledgements

This project has received funding from the European Research Council (ERC) under the European Union's Horizon 2020 research and innovation programme (grant agreement No 810207 to M.W.). L.C. was supported by the European Union's Horizon 2020 Marie Sklodowka-Curie individual fellowship program (H2020-MSCA-IF-101028239 – MolecularArp). A.J. was supported by the Fondation Bettencourt-Schueller (Impulscience program). G. R.-L. was supported by the Fondation pour la Recherche Medicale (grant EQU202203014630). MW is supported by the Francis Crick Institute, which receives its core funding from Cancer Research UK (CC2096), the UK Medical Research Council (CC2096), and the Wellcome Trust (CC2096). M.V. and S.B. are supported by funding from the French National Research Agency (ANR) grant Equipex+ IDEC (France 2030 investment plan ANR-21-ESRE-0002) and the France-BioImaging infrastructure (ANR-10-INBS-04). We thank Jean-Jacques Honorine (Institut Fresnel, France) for technical help with the calibration of the polarized fluorescence microscope. We acknowledge the Photonics facility of the

Institut Fresnel. We thank Jeremy Carlton (King's College London, UK) and Klemens Rottner (Helmholtz Centre for Infection Research, Germany) for feedback on the manuscript. For the purpose of Open Access, the authors have applied a CC BY public copyright licence to any Author Accepted Manuscript version arising from this submission.

Competing interests statement

The authors declare that they have no competing interests.

Figure Legends

Figure 1. SPIN90 selectively activates ArpC5L containing Arp2/3 complexes

(A) SPIN90 efficiently activates ArpC5L but not ArpC5 containing Arp2/3 complexes. Representative plots of pyrene-actin polymerization assays with 10 nM Arp2/3 complex, 100 nM SPIN90 and 2.5 µM actin (5 % pyrene labelled). It demonstrates that ArpC5L- but not ArpC5-containing Arp2/3 complexes activated by SPIN90 induce rapid actin polymerization, regardless of the ArpC1 isoform. The experiments were repeated independently three times and yielded similar results.

(B) Representative TIRF images demonstrate that ArpC5L- but not ArpC5-containing complex activated by SPIN90 efficiently generate actin filaments. Scale bar = 20 µm A mixture of 20 nM Arp2/3 complex, 200 nM SPIN90 and 0.5 µM actin (15 % Alexa 488 labelled) was observed overtime. The graph shows quantitative analysis of filament density over time from three independent technical replicates. The points indicate the mean density, and the error bars represent the standard deviation.

Figure 2. SPIN90 has a higher affinity for Arp2/3 complexes with ArpC5L than ArpC5

(A) Surface representation of the Arp2/3 complex from the SPIN90-Arp2/3 complex structure (PDB: 6DEC). Residues in Arp2/3 complex subunits contacting the two SPIN90 molecules are shown in darker colours.

(B) Immunoblots using an ArpC2 antibody show the amount of Arp2/3 complex containing ArpC1B pulled down with GST–SPIN90-Cter. Both blots were run on the same gel and developed on the same membrane to allow a direct comparison of signal intensity.

(C) The graph shows the quantification of average normalized ArpC2 intensity from three independent replicates, with error bars resenting standard deviation. The data was fit with Hill equation.

Figure 3. SPIN90 localizes at the leading edge and integrates into lamellipodial actin networks.

(A) Quantitative immunoblot analysis of endogenous levels of ArpC5 isoforms in B16 cells using recombinant His-tagged ArpC5 and His-tagged ArpC5L as standards. The average concentrations and standard deviations from three independent replicates are shown in the table on the right.

(B) Schematic shows the two Ruby-tagged SPIN90 constructs expressed in cells. Representative live images show B16 cells overexpressing GFP (volume marker) together with Ruby–SPIN90 (upper) or with Ruby-SPIN90 Nter (lower). Scale bars = 5 µm. Signal intensity (right) is quantified by normalizing the intensity at the leading edge (solid line) compared to that 2 µm from the leading edge (dashed line). Each pair of points represents measurements from the same cell with the different colours representing data from three

independent replicates. A two-tailed paired t-test is used to estimate the p-value.

Figure 4. SPIN90 integrates into the lamellipodia with Arp2/3 complex

(A) Representative maximum intensity projection over 14 seconds for cells expressing endogenous NeonGreen–ArpC5L, together with overexpressed Ruby–SPIN90 or Ruby–SPIN90-Nter. ArpC5L and Ruby–SPIN90, but not Ruby–SPIN90-Nter undergo rearward movement in the lamellipodium (highlighted with yellow arrows). The similar trajectory pattern observed in all the cells (20 for SPIN90-FL and 13 for SPIN90-Nter) across three independent replicates.

(B) Representative live image (upper) of B16 cells with endogenously labelled NeonGreen-ArpC5L and overexpressing Ruby–SPIN90. Kymographs (lower), generated from the orange lines in the upper images, show that ArpC5L (left) and SPIN90 (right) exhibit directional movement, highlighted with blue arrows. Quantitative analysis (right panel) of the rearward flow of ArpC5L and SPIN90 respectively. Different colours indicate results from three independent replicates. A two-tailed unpaired t-test with Welsh's correction is used to estimate the p-value. Scale bars = 5 µm

Figure 5. SPIN90 enhances the recruitment of ArpC5L but not ArpC5 to the leading edge

Representative images of live cells expressing endogenous NeonGreen–ArpC5L (A) or ArpC5-NeonGreen (B) after treatment with the indicated siRNAs. Allstar represents siRNA control. The graphs show quantification of the ArpC5L or ArpC5 signal intensity at the leading edge in the different conditions. Each point represents an individual cell, with different colours indicating 3 independent experimental replicates. For each repeat, 8-15 cells were imaged and quantified. The mean of each experiment is shown as a circle, and error bars are standard deviation. A two-tailed paired t-test was used to calculate the p-value. Scale bars = 5 µm

Figure 6. The organisation of actin filaments at the leading edge of B16 cells.

(A) Schematic representation of ρ (rho) and ψ (psi) in the organization of the actin network.

(B) Representative images of an Alexa-488 phalloidin stained B16 cell for each cell line as indicated. The coloured region in the lamellipodium is the result of polarimetry analysis within a 0.65 µm (10-pixel) region from the leading edge to determine the mean actin filament orientation in each pixel. The mean filament orientation per pixel is represented with a stick whose orientation corresponds to filament orientation (angle rho, ρ) and whose color depicts filament orientation with respect to the leading edge (angle rho_c, ρ_c) within the

0–180° range according to the colour bar. The stick maps of a representative ROI (labelled with white rectangles) are zoomed in and shown.

(C) The polar histogram shows the statistical distribution of actin filament angles (ρ_c) per pixel within the 0–90° range relative to the leading edge of all the cells, with 38 to 55 cells analysed per condition across three independent repeats. The average $< \rho_c >$ and standard deviation for each cell line are indicated. The colours correspond to the colour bar shown in panel A.

(D) Violin plot showing the statistical distribution of actin filament angles (ρ_c) per pixel within the 0–90° range, as shown in panel B. A two-tailed Mann–Whitney test was used to calculate the p-value between individual cells under two conditions. The medians and interquartile ranges are shown as black lines, while the means and standard deviations are shown as blue dots with error bars.

(E) The statistical results of the average lamellipodial actin filament angle $< \rho_c >$ relative to the leading edge within the 0–90° range in individual wildtype, ArpC5, ArpC5Lor SPIN90 knockout cells. Each point represents the mean angle of actin filaments relative to the leading edge in a single cell from three independent experiments, the latter shown in different colours. Mean ± SD for each experimental condition is indicated. A two-tailed Welch's t-test is used to estimate the p-value between the means under two conditions.

(F) The statistical results of the standard deviation (SD) of actin filament angles relative to the leading edge within the 0–90° range in individual wildtype, ArpC5, ArpC5L, or SPIN90 knockout cells. Each point represents the SD of actin filaments relative to the leading edge in a single cell from three independent experiments, the latter shown in different colours. Mean ± SD for each experimental condition is indicated. A two-tailed Mann Whitney test is used to estimate the p-value between individual cells under two conditions.

(G) Representative images of Alexa-488 phalloidin stained B16 cell (right) overexpressing Ruby-SPIN90 (left). The zoomed-in image shows the mean actin filament orientation per pixel within the ROI (white rectangle) as in panel A.

(H) The polar histogram shows the statistical distribution of actin filament angles (ρ_c) per pixel within the 0–90° range relative to the leading edge in all cells overexpressing either Ruby-SPIN90 (61 cells) or Ruby-SPIN90 Nter (59 cells), across three independent experimental repeats. The average $< \rho_c >$ and standard deviation for each experimental condition are indicated. The colours correspond to the colour bar shown in panel A.

Figure 7. SPIN90 impacts the lamellipodia protrusion and cell motility.

(A) Representative image stills of WT, ArpC5, ArpC5Land SPIN90 knockout B16 cells expressing endogenously tagged GFP β-actin.

(B) The quantification of lamellipodia width, lamellipodial actin density. Each point represents an individual cell, with different colours indicating independent experimental replicates. The mean of each experiment is shown as a circle,

and error bars are standard deviation. A two-tailed paired t-test was used to estimate the p-value between the means under two conditions.

(C) Representative image still (upper) from a FRAP assay on a B16 cell with endogenously GFP tagged β–actin. The kymograph (lower) shows the cell protrusion (indicated by straight line) and rearward flow (indicated by dashed line), made visible by the FRAP region.

(D) The quantification of lamellipodial protrusion rate, rearward flow and protrusion efficiency. Each point represents an individual cell, with different colours indicating independent experimental replicates. The mean of each experiment is shown as a circle, and error bars are standard deviation. A two-tailed paired t-test was used to estimate the p-value between the means under two conditions.

(E) Quantification of B16 cell random migration speed. Each point represents an individual cell, with different colours indicating 3 independent replicates. The mean of each experiment is shown as a circle, and error bars represent standard deviation. A two-tailed paired t-test was used to estimate the p-value between the means under two conditions.

(F) Representative images (left panels) of the leading edge of B16 cells overexpressing either Ruby, or Ruby-SPIN90. The right panel shows the protrusion rate of these cells. Each point represents an individual cell, with different colours indicating independent experimental replicates. The mean of each experiment is shown as a circle, and error bars are standard deviation. A two-tailed paired t-test was used to estimate the p-value between the means under two conditions.

Figure 8. Schematic summary

(A) In migrating cells, SPIN90 recruits the ArpC5L-, but not the ArpC5-containing complex, to the lamellipodial leading edge (1). Meanwhile, both ArpC5L- and ArpC5-containing complexes generate branches at the lamellipodia (2). Thus, SPIN90 and Arp2/3 iso-complexes integrate into the lamellipodial actin network, contributing to the formation of a complex actin architecture that ensures efficient protrusion (3).

(B) ArpC5 KO cells (left panel), the ArpC5L-containing complex participates in the formation of both linear and branched actin filaments. Consequently, the distribution of filament orientations in their lamellipodia is much fig than that of the wild type. In contrast, in ArpC5L KO cells (right panel), the ArpC5-containing complex generates only branched actin filaments, resulting in a narrower distribution of filament orientations.

Supplementary Figure legends

SF 1. Binding between the Arp2/3 complex and SPIN90.

(A) Sequence alignment between ArpC5 and ArpC5L subunit. The interface binding SPIN90 is highlighted with colours: residues that are identical in both isoforms are shown in yellow, while distinct residues are shown in cyan.
(B) Immunoblot using an ArpC2 antibody demonstrate that ArpC5L-containing Arp2/3 complexes interact more strongly with GST–SPIN90-Cter than those with ArpC5.
(C) The immunoblot showing the results in Fig. 2C were developed on the same blot.

SF 2. The western blot of siRNA treated cells.

(A) The western blot of siRNA treated ArpC5-NeonGreen B16 cells.
(B) The western blot of siRNA treated NeonGreen-ArpC5L B16 cells.

SF 3. The organisation of lamellipodial actin.

(A) Corresponding to Fig 6A, B. Representative images of an Alexa-488 phalloidin stained B16 cell for each cell line as indicated. The mean filament orientation per pixel is represented with a stick whose orientation corresponds to filament orientation (angle rho, ρ) and whose colour depicts filament alignment (angle psi, ψ) according to the colour bar. The stick maps of a representative ROI (labelled with white rectangles) are zoomed in and shown.
(B) The histogram shows the statistical distribution of filament alignment angles ψ per pixel of all the individual cells, with 38 to 55 cells analysed per condition across three independent repeats. The average <ψ> and SD for each cell line are indicated. The colours correspond to the colour bar shown in panel A.
(C) Statistical analysis of the average <ψ> in each individual wildtype, ArpC5, and ArpC5L or SPIN90 knockout cells. Mean ± SD for each cell line is indicated. A two-tailed Welch's t-test is used to estimate the p-value between individual cells under two conditions.
(D) Corresponding to Fig 6C. The polar histogram shows the statistical distribution of actin filament angles (ρ_c) per pixel within the 0–180° range relative to the leading edge in all cells. The average ρ_c per pixel and SD for each cell line are indicated. The colours correspond to the color bar shown in panel Fig 6A.
(E) Corresponding to Fig. 6H. The polar histogram shows the statistical distribution of actin filament angles (ρ_c) per pixel within the 0–180° range relative to the leading edge in all cells, overexpressing either Ruby-SPIN90 or Ruby-SPIN90 Nter. The average $< \rho_c >$ and standard deviation for each experimental condition are indicated.
(F) The statistical results of the average lamellipodial actin filament angle relative to the leading edge within the 0–90° range in individual wildtype cells (also shown in Fig. 6H) or cells overexpressing either Ruby-SPIN90 or Ruby-SPIN90 Nter. Each point represents the mean angle of actin filaments relative to the leading edge in a single cell from three independent experiments, the latter shown in different colours. Mean ± SD for each experimental condition is

indicated. A two-tailed Welch's t-test is used to estimate the p-value between the means under two conditions.

SF 4. Analysis of KO cell lines.

(A) The left panel shows the absence of targeted gene, while the right panel show the endogenous labelling of GFP-β-actin in these cell lines.
(B) The graphs show quantification of the polymerization rate which is calculated by summing the rearward flow and protrusion rates. Each point represents an individual cell, with different colours indicating independent experimental replicates. The mean of each experiment is shown as a circle, and error bars indicated the standard deviation. A two-tailed paired t-test was used to calculate the p-value between the means under two conditions.

Movie legends

Movie 1. Movie showing live imaging of B16 cells overexpressing GFP (a volume marker) and Ruby-SPIN90, corresponding to Fig. 3B (middle panel). The right panel shows inverted-intensity live images of each channel. Scale bars 5 µm

Movie 2. Movie showing live imaging of B16 cells overexpressing GFP (a volume marker) and Ruby-SPIN90 Nter, corresponding to Fig. 3B (lower panel). The right panel shows inverted-intensity live images of each channel. Scale bars 5 µm

Movie 3. Movie showing live imaging of NeonGreen-ArpC5L B16 cells overexpressing Ruby-SPIN90, corresponding to Fig. 4A (upper panel). The middle and the right panel show inverted-intensity live images of each channel. Scale bars 5 µm

Movie 4. Movie showing live imaging of NeonGreen-ArpC5L B16 cells overexpressing Ruby-SPIN90, corresponding to Fig. 4A (lower panel). The middle and the right panel show inverted-intensity live images of each channel. Scale bars 5 µm

Materials and Methods

Protein purification and preparation

Recombinant human Arp2/3 iso-complexes with defined composition (Uniprot P61160, P61158, Q92747, O15143, O15144, O15145, P59998, Q9H9F9 and Q98PX5) were purified as previously reported (*41*). In this study, we focus on the Arp2/3 complex with Arp3 background because our previous study showed that both Arp3B and Arp3 containing Arp2/3 complex can generate linear filaments with SPIN90 (*32*). Skeletal muscle α-actin was purified from rabbit muscle following the published protocol (*42*). GST-tagged and untagged human SPIN90 C-terminus (267-715, UniProt Q9NZQ3-3) were purified as previously reported (*43*). Similarly, GST-tagged and untagged mouse SPIN90 full length (UniProt Q9ESJ4) were purified. Actin was fluorescently labelled on its lysine 328, with Alexa-488 succinimidyl ester (Life Technology) following the reported protocol (*44*). Actin was labelled with N(1-pyrene)-iodoacetamide (Thermo Fisher Scientific) as previously described (*45*).

Pyrene actin polymerization assay

To probe actin polymerization, 100 nM SPIN90-Cter and 10 nM Arp2/3 iso-complexes were mixed with 2.5 μM Actin (5% pyrene labelled) and loaded immediately on a Safas Xenius fluorimeter. The negative control experiment was done without SPIN90-Cter. The experiments were performed at room temperature with a buffer containing 5 mM Tris-HCl pH 7.0, 0.1 mM CaCl2, 0.2 mM ATP, 50 mM KCl, 1 mM $MgCl_2$, 0.2 mM EGTA and 1 mM DTT.

TIRF assays

The coverslips were treated with Deep UV and passivated by mPEG silane overnight. The passivated coverslips were rinsed thoroughly with ethanol and water. Then they were dried and stuck to the glass slides with 3-mm-separated parafilm bands to create flow chambers. The experiments were performed at 25 °C. To begin with, 200 nM SPIN90-Cter, 20 nM Arp2/3 iso-complexes were mixed in a buffer containing 5 mM Tris-HCl pH 7.0, 50 mM KCl, 1 mM $MgCl_2$, 0.2 mM EGTA, 0.2 mM ATP, 10 mM DTT, 1 mM DABCO, 0.1% BSA, and 0.3% Methylcellulose 4000 cP. The moment when 0.5 μM G-actin (15% Alexa-488 labelled) was added to the system was recorded as time 0. Negative control experiments were performed using the same system, either without SPIN90-Cter or with actin alone. For each condition, a random field of view was selected to quantify actin density. Actin density was quantified as the number of actin filaments divided by the surface area of the selected region.

GST pull-down assays

The Glutathione Sepharose™ 4B resin (GE Healthcare) was incubated with 5% BSA for 5 min and washed three times with GST pull-down buffer containing 50 mM Tris-HCl pH 7.0, 50 mM KCl, 1 mM $MgCl_2$, 0.2 mM EGTA, 0.2 mM ATP, 1 mM DTT, and 5% glycerol. The beads were then incubated with 20 μM GST-SPIN90-Cter or 20 μM GST at 4 °C for 1h, followed by incubation with 100 nM Arp2/3 iso-complexes at 4 °C for 30 min. The beads were washed three times with 300 μL GST pull-down buffer. The proteins attached to the beads were eluted with 50 μL of 50 mM reduced glutathione. The sample was analyzed by SDS-PAGE followed by western blot using Anti-ArpC2 (sigma) to detect Arp2/3 complexes. Amersham imager AI600 or ImageQuant™ 800 was used to develop the western blot results. "To quantify the affinity between SPIN90 and Arp2/3 iso-complexes, we focused on Arp2/3-ArpC1B-ArpC5 and Arp2/3-ArpC1B-ArpC5L. Equal amounts of SPIN90-coated GST beads were incubated with varying concentrations of Arp2/3 iso-complexes. The

amounts of eluted Arp2/3-ArpC5 and Arp2/3-ArpC5L were loaded onto the same gel and transferred to the same western blot membrane. The developed western blot was analyzed using FIJI with plugin GelAnalyzer. The experiments were repeated independently three times, and all the results were included in the final plot (Fig. 2C).

Antibody, immunoblot analysis

The antibody against mouse SPIN90 (UniProt Q9ESJ4) was generated by immunizing rabbits with full-length purified recombinant mouse SPIN90 protein (WhiteAntibodies). Other antibodies are including: ARPC2/p34-Arc polyclonal (Millipore, 07-227), ARPC5 monoclonal (Synaptic Systems, 305011), ArpC5L (Proteintech, 22025-a-AP), β-actin (Abcam, ab179467), anti-mouse IgG-IRDye® 800CW (LI-COR Biosciences, 926-32210) and anti-rabbit IgG-IRDye® 680RD (LI-COR Biosciences, 926-68071). Unless otherwise specified, western blot results were developed on LI-COR Odyssey CLx imaging system. FIJI with plugin GelAnalyzer was used to analyse the results.

Cell culture and cell lines

WT M. Musculus B16-F1melanoma cells were gifts from Klemens Rottner lab (*36*). Unless otherwise specified in this project, cells were cultured in Gibco DMEM (ThermoFisher, 41966-029) with additional 10% FBS (CAPRICORN, FBS-LE-12A) and 1% Penicillin-Streptomycin (P/S, ThermoFisher, 15140122) at 37°C and 5% CO_2. To detach the cells, cells were washed with PBS once and then treated with 0.25% Trypsin-EDTA (ThermoFisher, 25200056) at room temperature for 2-3 minutes.

ArpC5, ArpC5L and SPIN90 KO cell lines were generated by GRSPR-Cas9-mediated genome editing approaches. In each case, to generate a cut in the target gene, a pair of guide RNA were cloned intro pSpCas9(BB)-2A-Puro (Addgene, ID 48139) respectively and introduced into B16-F1 at the same time. The ArpC5 guide RNAs are ‘GACCGGGCTGGGCTCGCTAA’ and ‘GCGAGGTGGACTCGTGCCTA’. The guide RNAs against ArpC5L are ‘ATTCGTCGATATCCACGCGG’ and ‘CGGCAATATCCTTCCCGGCG’. The SPIN90 guide RNAs are ‘GAGAGCCTAGAAGTCTGCAT’ and ‘GCTCCGTGGTGTCCATTGGA’. Cells were transfected using Fugene® HD Transfection Reagent. The next day, cells were selectively cultured by introducing 2.5 µg/mL puromycin into the medium. After 3 days, surviving cells were trypsinized and resuspended in PBS with additional 5% FBS. The single cells were sorted by the flow cytometry and seeded in DMEM with additional 20% FBS and 1% P/S in 96 well plates. Two weeks later, single colonies were expanded for characterizing, including Western blot and genomic sequencing of the target loci.

ArpC5 and ArpC5L genes were modified using ORANGE, a CRISPR-Cas9–mediated genome editing toolbox to fuse a NeonGreen tag with the target gene (*46*). pOrange NeonGreen-ArpC5 KI plasmid was modified based on pOrange GFP-ArpC5 KI (Addgene #131503). pOrange ArpC5L-NeonGreen KI plasmid was generated using the guide RNA: ‘CAGTGTGTTCCGGGCCATGG’. The same method was used to generate endogenously GFP-tagged β-actin. The plasmid pOrange GFP-Actb KI (Addgene #131479) was transfected into the WT, ArpC5 isoform KO, SPIN90 KO cells respectively. Single cells with green fluorescence were sorted by flow cytometry and seeded into 96-well plates containing DMEM supplemented with 20% FBS and 1% P/S. Expanded single colonies were examined by Western blot. All the positive clones we tested (approximately 10 for each condition) were heterozygous.

B16 cells overexpressing GFP was generated using lentivirus infection (Trono group second generation packaging system, Addgene) and selected using puromycin resistance (1 µg/mL) as previously described (*21*).

siRNA transfection

All-Star control (Qiagen, SI03650318) was used as the control. The following RNAi were purchased from Dharmacon (SMARTPools): siGENOME mouse ArpC5 (NM_026369), siGENOME mouse ArpC5L (NM_028809), siGENOME mouse NCKIPSD/SPIN90 (NM_030729). The final concentration of 20 nM was used. The cells were transfected with HiPerFect (Qiagen) using the fast forward method in 6-well plates. The experiments were performed 48h after the transfection. At the same time, the depletion of target gene were examined with Western Blot.

Polarized fluorescence microscopy on fixed cells

B16 cells were seeded on laminin coated coverslips as previously reported (*24*), and cultured in CO_2 independent medium (Gibco™) with additional 10% FBS and 2 mM L-Glutamine at 37°C. After 3h30 incubation, the cells were fixed with 0.35% glutaraldehyde and 4% PFA in cytoskeleton buffer at 37°C, as reported (*47*). The samples were washed twice with PBS containing 1 mg/mL sodium borohydride and three times with PBS. The actin cytoskeleton was stained with 0.22 µM Phalloidin Alexa-488 at room temperature for 2 h in PBS containing 0.1% saponin and 10% BSA. The samples were mounted with Mowiol and kept at 4 °C.

The images were acquired using a custom spinning disk polarization-resolved fluorescence microscope with a Nikon Plan Apo ×100/1.45 NA oil immersion objective lens, 488- and 561-laser lines and an iXon Ultra 888 EMCCD camera, described in detail in Martins et al, 2025. Polarized image stacks using 18 polarization angles with steps of 10° were recorded with an exposure time of 0.3-0.4 s per polarized image. Analysis and data representation, including color-coded stick representations of ρ angles with respect to the leading edge (ρ_c) and of ψ angles per pixel, histograms and polar histograms were generated with the open source PyPOLAR software (RRID:SCR_024681) (Martins et al, 2025). Pixels of the lamellipodia selected for analysis were identified using a combination of intensity thresholding and the "edge detection" tool in PyPOLAR to detect the leading edge and manual region selection, excluding microspikes. Only 10 pixels (0.65 µm) from the leading edge were included for analysis.

Live cell imaging

The siRNA treated NeonGreen-ArpC5 and ArpC5L-NeonGreen cells were seeded on laminin-coated coverslips in Leibovitz's L-15 medium supplemented with 10% FBS and 2 mM L-glutamine at 37 °C. After 3-hour incubation, the cells were imagined on a Zeiss Axio Observer spinning disc with a Plan Achromat 100x/1.46 NA oil lens, an Evolve 512 camera, and a Yokagawa CSUX spinning disk. The microscope was controlled by the SlideBook software (3i Intelligent imaging Innovations). For each condition, more than 8 cells with lamellipodia were chosen randomly. The same exposure time, 200 ms, was applied in each acquisition. Similarly, WT and KO cells expressing endogenous GFP-β-actin were seeded and imagined on the confocal spinning disc with a Plan Achromat 100x/1.46 NA oil lens. Life images were acquired at 5 second intervals. A region of interest on the lamellipodia was photobleached using a focused 3-ms pulse of a 405 nm laser. Images were analyzed using FIJI software with Multi Kymograph.

Ruby-tagged SPIN90 was transiently introduced into cells using the FuGENE kit 48 hours before the experiment. The ArpC5L-NeonGreen or GFP overexpressing Ruby-tagged SPIN90 cells were seeded on laminin-coated coverslips in Leibovitz's L-15 medium supplemented with 10% FBS and 2 mM L-glutamine at 37 °C. After 3 hours, the cells were imagined using instant Structured Illumination Microscopy (VT-iSIM). VT-iSIM was conducted on an Olymus iX83 Microscope with Olympus 150x/1.45 NA X-Line apochromatic objective lens, dual Photometrics BSI-Express sCMOS cameras, and CoolLED pE-300 light source (Visitech), controlled using Micro-Manager. Images were acquired at 1 second intervals with 200 ms exposure time. Images were analyzed using FIJI software. Normalized fluorescent signal intensity at the leading edge was quantified by dividing the intensity at the leading edge (solid line, Fig. 3A) by the intensity measured 2 µm behind the leading edge (dashed line, Fig. 3A).

To quantify the random motility, WT and CRISPR KO cells were imaged and analysed using the Livecyte system (PhaseFocus) every 10 minutes for 16 hours at 10x. The imaging chamber was maintained at 37 °C with 5% CO_2. Livecyte automatically process the data and quantified the cell motility.

Protein structure analysis

Pymol is used to visualise and analyse the structure of SPIN90 bound Arp2/3 (*48*).

Statistical analysis

Statistical analyses were performed with Prism 10 (Version 10.1.1). Sample numbers, mean and P value can be found in the figures or figure legends. Unless otherwise specified, each experiment have been independently repeated three times. P-values smaller than 0.05 are considered statistically significant. Moreover, Cohen's d was also used to assess the effect size; a Cohen's d greater than 0.8 is considered a large effect. Cells receiving the treatment (e.g., siRNA) on the same day were paired. A paired two-tailed Student's t-test was then used to compare the means between the two groups. Also, a paired two-tailed Student's *t*-test was used to compare the signal intensity of GFP and Ruby SPIN90 at the leading edge. Because the data distribution in the polarized microscopy assay differs substantially, we used an unpaired two-tailed *t*-test with Welch's correction or Mann Whitney test to compare the two groups. A paired two-tailed *t*-test with was used to compare the cell motility and lamellipodia protrusion between wild type and KO cell lines.

Supplementary:

Sequence results:

<u>The grey colored fragment is present in WT cell lines but missing in KO cells.</u>

B16-F1 ArpC5 knockout lines

Reference: MmC5 WT

CCGGGCTGGGCTCGCTAAAGGAGAGGCACCGCGGAGGGGCAGGCCAGCGTCGCGTCGCGATCCGGGATGTC
GAAGAACACGGTGTCGTCGGCCCGCTTCCGGAAGGTGGACGTGGACGAATATGACGAGAACAAGTTCGTGG
ACGAGGAGGACGGCGGCGATGGCCAGGCCGGGCCCGACGAGGGCGAGGTGGACTCGTGCCTACGGCAATA
TC

MmC5 KO 2.1

CCGGGCTGGGCTCGCGCGGCAATATC

B16-F1 ArpC5L Knockout lines

Reference: MmC5L WT

CGCTTCCGCCGCGTGGATATCGACGAATTTGACGAGAACAAATTCGTAGACGAGCACGAAGAGGCAGCGGC
GGCGGCGGGCGAGCCAGGCCCCGACCCCTGCGAGGTAGACGGGCTCCTGCGGCAATATCCTTCCCGGCGCG
GCGGCCCGGCT

MmC5L KO 2.2

CGCTTCCGCCGCGTGGCGCGGCGGCCCGGCT

B16-F1 SPIN90 Knockout lines

Reference: SPIN90 WT

GAGGATGGCCTTCCAATGGACACCACGGAGCAGCTGCCAGACCTCTGCATGAACCTGCTTCTGGCTCTCAACC
TGCACCTGACAGGTGGGGTGGGGCCATCTGGAAGGCAGCTGAGCAGTGGGCTTTTCGGGCTTCGCGGGCTTC
TGTGCCTACACTCTTACCTGTCTCCATCCACGTCTCTCCGCAGCTCCTGAGCAGAATGTCATCATGGCTGCCTTG
AGCAGACACACCAATGTGAAGATCTTCTCTGAGAAGCTGCTTCTGCTTCTGAACAGAGGGGGTGAGAGCCTA
GAAGTCTGCATGGGTGCCGCTTGCGT

SPIN90 KO 2.10

GAGGATGGCCTTCCCATGGGTGCCGCTTGCGT

References

1. L. M. Machesky *et al.*, Mammalian actin-related protein 2/3 complex localizes to regions of lamellipodial protrusion and is composed of evolutionarily conserved proteins. *Biochem J* **328**, 105-112 (1997).
2. V. Papalazarou, L. M. Machesky, The cell pushes back: The Arp2/3 complex is a key orchestrator of cellular responses to environmental forces. *Curr Opin Cell Biol* **68**, 37-44 (2021).
3. M. D. Welch, A. H. DePace, S. Verma, A. Iwamatsu, T. J. Mitchison, The human Arp2/3 complex is composed of evolutionarily conserved subunits and is localized to cellular regions of dynamic actin filament assembly. *J Cell Biol* **138**, 375-384 (1997).
4. T. E. B. Stradal, M. Boiero Sanders, P. Bieling, Arp2/3-complex regulation - Novel insights and open questions. *Curr Opin Cell Biol* **95**, 102565 (2025).
5. L. Cao, M. Way, The stabilization of Arp2/3 complex generated actin filaments. *Biochem Soc Trans* **52**, 343-352 (2024).
6. A. M. Gautreau, F. E. Fregoso, G. Simanov, R. Dominguez, Nucleation, stabilization, and disassembly of branched actin networks. *Trends Cell Biol* **32**, 421-432 (2022).
7. R. D. Mullins, J. A. Heuser, T. D. Pollard, The interaction of Arp2/3 complex with actin: nucleation, high affinity pointed end capping, and formation of branching networks of filaments. *Proc Natl Acad Sci U S A* **95**, 6181-6186 (1998).
8. A. R. Wagner, Q. Luan, S. L. Liu, B. J. Nolen, Dip1 defines a class of Arp2/3 complex activators that function without preformed actin filaments. *Curr Biol* **23**, 1990-1998 (2013).
9. S. Espinoza-Sanchez, L. A. Metskas, S. Z. Chou, E. Rhoades, T. D. Pollard, Conformational changes in Arp2/3 complex induced by ATP, WASp-VCA, and actin filaments. *Proc Natl Acad Sci U S A* **115**, E8642-E8651 (2018).
10. B. A. Smith *et al.*, Three-color single molecule imaging shows WASP detachment from Arp2/3 complex triggers actin filament branch formation. *Elife* **2**, e01008 (2013).
11. N. Molinie *et al.*, Cortical branched actin determines cell cycle progression. *Cell Res* **29**, 432-445 (2019).

12. Q. Luan, S. L. Liu, L. A. Helgeson, B. J. Nolen, Structure of the nucleation-promoting factor SPIN90 bound to the actin filament nucleator Arp2/3 complex. *EMBO J* **37**, (2018).
13. L. Cao *et al.*, SPIN90 associates with mDia1 and the Arp2/3 complex to regulate cortical actin organization. *Nat Cell Biol* **22**, 803-814 (2020).
14. C. Hinze, E. Boucrot, Endocytosis in proliferating, quiescent and terminally differentiated cells. *J Cell Sci* **131**, (2018).
15. B. R. Schrank *et al.*, Nuclear ARP2/3 drives DNA break clustering for homology-directed repair. *Nature* **559**, 61-66 (2018).
16. C. Wu *et al.*, Arp2/3 is critical for lamellipodia and response to extracellular matrix cues but is dispensable for chemotaxis. *Cell* **148**, 973-987 (2012).
17. C. J. Balzer, A. R. Wagner, L. A. Helgeson, B. J. Nolen, Single-Turnover Activation of Arp2/3 Complex by Dip1 May Balance Nucleation of Linear versus Branched Actin Filaments. *Curr Biol* **29**, 3331-3338 e3337 (2019).
18. R. C. Robinson *et al.*, Crystal structure of Arp2/3 complex. *Science* **294**, 1679-1684 (2001).
19. P. Jay *et al.*, ARP3beta, the gene encoding a new human actin-related protein, is alternatively spliced and predominantly expressed in brain neuronal cells. *Eur J Biochem* **267**, 2921-2928 (2000).
20. T. H. Millard, B. Behrendt, S. Launay, K. Futterer, L. M. Machesky, Identification and characterisation of a novel human isoform of Arp2/3 complex subunit p16-ARC/ARPC5. *Cell Motil Cytoskeleton* **54**, 81-90 (2003).
21. J. V. Abella *et al.*, Isoform diversity in the Arp2/3 complex determines actin filament dynamics. *Nat Cell Biol* **18**, 76-86 (2016).
22. W. Roman *et al.*, Myofibril contraction and crosslinking drive nuclear movement to the periphery of skeletal muscle. *Nat Cell Biol* **19**, 1189-1201 (2017).
23. L. Sadhu *et al.*, ARPC5 isoforms and their regulation by calcium-calmodulin-N-WASP drive distinct Arp2/3-dependent actin remodeling events in CD4 T cells. *Elife* **12**, (2023).
24. F. Fassler *et al.*, ArpC5 isoforms regulate Arp2/3 complex-dependent protrusion through differential Ena/VASP positioning. *Sci Adv* **9**, eadd6495 (2023).
25. W. H. Kahr *et al.*, Loss of the Arp2/3 complex component ARPC1B causes platelet abnormalities and predisposes to inflammatory disease. *Nat Commun* **8**, 14816 (2017).
26. S. Volpi *et al.*, A combined immunodeficiency with severe infections, inflammation, and allergy caused by ARPC1B deficiency. *J Allergy Clin Immunol* **143**, 2296-2299 (2019).
27. E. Sindram *et al.*, ARPC5 deficiency leads to severe early-onset systemic inflammation and mortality. *Dis Model Mech* **16**, dmm050145 (2023).
28. L. Vasconcellos, S. Huang, A. Suarez-Bonnet, S. Priestnall, M. L. W. Sunita Varsani-Brown, Kathleen Shah, Naoko Kogata, Brigitta Stockinger, Michael Way, Branched actin networks in innate immune cells mediate host microbiota homeostasis. *BioRXiv*, (2024). https://doi.org/10.1101/2024.07.18.604111
29. C. J. Nunes-Santos *et al.*, Inherited ARPC5 mutations cause an actinopathy impairing cell motility and disrupting cytokine signaling. *Nat Commun* **14**, 3708 (2023).

30. O. von Loeffelholz *et al.*, Cryo-EM of human Arp2/3 complexes provides structural insights into actin nucleation modulation by ARPC5 isoforms. *Biol Open* **9**, bio054304 (2020).
31. A. J. Saks, K. R. Barrie, G. Rebowski, R. Dominguez, NPF binding to Arp2 is allosterically linked to the release of ArpC5's N-terminal tail and conformational changes in Arp2/3 complex. *Proc Natl Acad Sci U S A* **122**, e2421557122 (2025).
32. L. Cao, S. Huang, A. Basant, M. Mladenov, M. Way, CK-666 and CK-869 differentially inhibit Arp2/3 iso-complexes. *EMBO Rep* **25**, 3221-3239 (2024).
33. C. Galloni *et al.*, MICAL2 enhances branched actin network disassembly by oxidizing Arp3B-containing Arp2/3 complexes. *J Cell Biol* **220**, (2021).
34. J. Francis *et al.*, Activation of Arp2/3 complex by a SPIN90 dimer in linear actin-filament nucleation. *Nat Struct Mol Biol*, doi: 10.1038/s41594-025-01673-8. Online ahead of print, (2025).
35. T. Liu *et al.*, Arp2/3-mediated bidirectional actin assembly by SPIN90 dimers. *Nat Struct Mol Biol*, doi: 10.1038/s41594-025-01665-8. Online ahead of print, (2025).
36. F. P. Lai *et al.*, Arp2/3 complex interactions and actin network turnover in lamellipodia. *EMBO J* **27**, 982-992 (2008).
37. A. Steffen *et al.*, Sra-1 and Nap1 link Rac to actin assembly driving lamellipodia formation. *EMBO J* **23**, 749-759 (2004).
38. C. S. Martins *et al.*, Genetically encoded reporters of actin filament organization in living cells and tissues. *Cell* **188**, 2540-2559 e2527 (2025).
39. N. Watanabe, T. J. Mitchison, Single-molecule speckle analysis of actin filament turnover in lamellipodia. *Science* **295**, 1083-1086 (2002).
40. G. Giannone *et al.*, Lamellipodial actin mechanically links myosin activity with adhesion-site formation. *Cell* **128**, 561-575 (2007).
41. L. Baldauf, F. Frey, M. Arribas Perez, T. Idema, G. H. Koenderink, Branched actin cortices reconstituted in vesicles sense membrane curvature. *Biophys J* **122**, 2311-2324 (2023).
42. J. A. Spudich, S. Watt, The regulation of rabbit skeletal muscle contraction. I. Biochemical studies of the interaction of the tropomyosin-troponin complex with actin and the proteolytic fragments of myosin. *J Biol Chem* **246**, 4866-4871 (1971).
43. L. Cao, F. Ghasemi, M. Way, A. Jegou, G. Romet-Lemonne, Regulation of branched versus linear Arp2/3-generated actin filaments. *EMBO J* **42**, e113008 (2023).
44. G. Romet-Lemonne, B. Guichard, A. Jegou, Using Microfluidics Single Filament Assay to Study Formin Control of Actin Assembly. *Methods Mol Biol* **1805**, 75-92 (2018).
45. J. A. Cooper, S. B. Walker, T. D. Pollard, Pyrene actin: documentation of the validity of a sensitive assay for actin polymerization. *J Muscle Res Cell Motil* **4**, 253-262 (1983).
46. J. Willems *et al.*, ORANGE: A CRISPR/Cas9-based genome editing toolbox for epitope tagging of endogenous proteins in neurons. *PLoS Biol* **18**, e3000665 (2020).
47. C. V. Rimoli, C. A. Valades-Cruz, V. Curcio, M. Mavrakis, S. Brasselet, 4polar-STORM polarized super-resolution imaging of actin filament organization in cells. *Nat Commun* **13**, 301 (2022).

48. Schrodinger, LLC. (2015). The PyMOL Molecular Graphics System, Version 1.8.

A

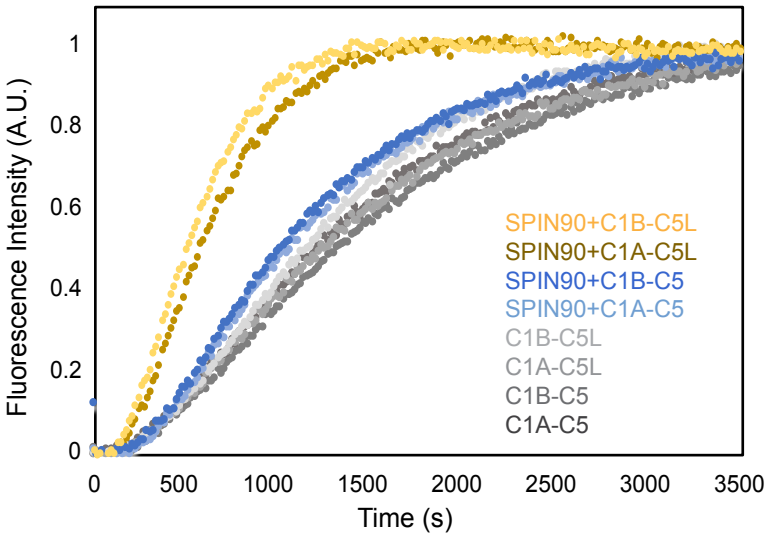

B

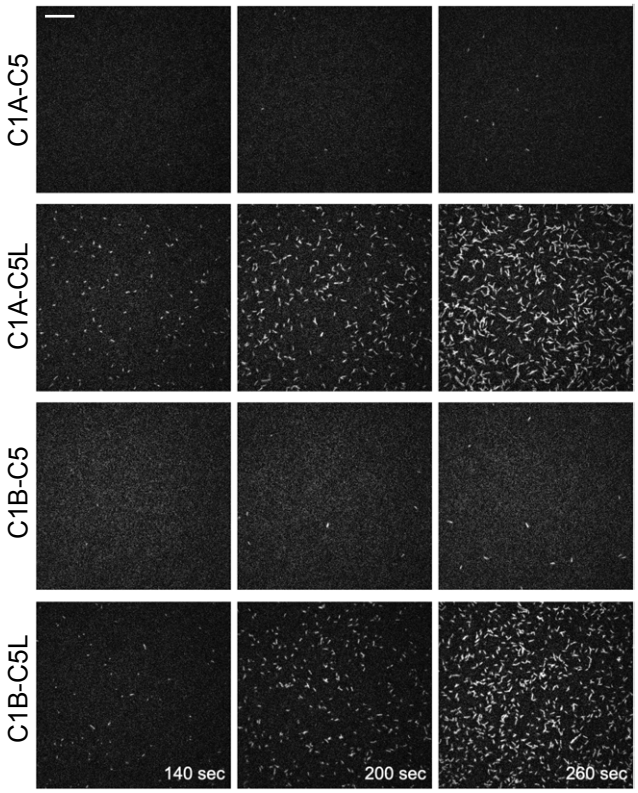

Scale bar = 20 µm

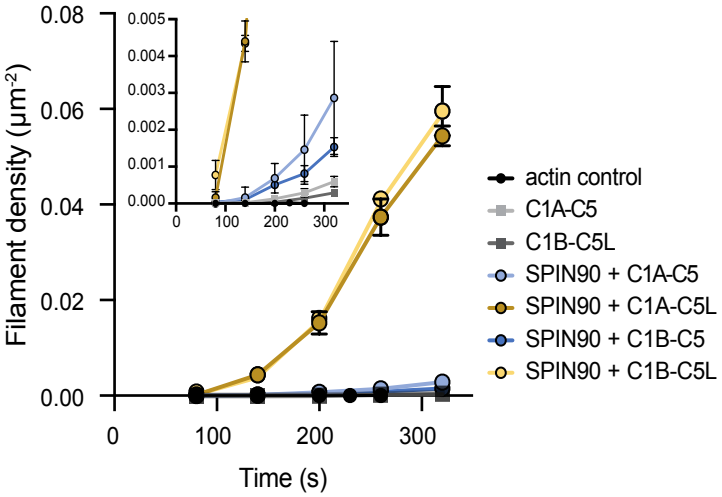

Figure 1

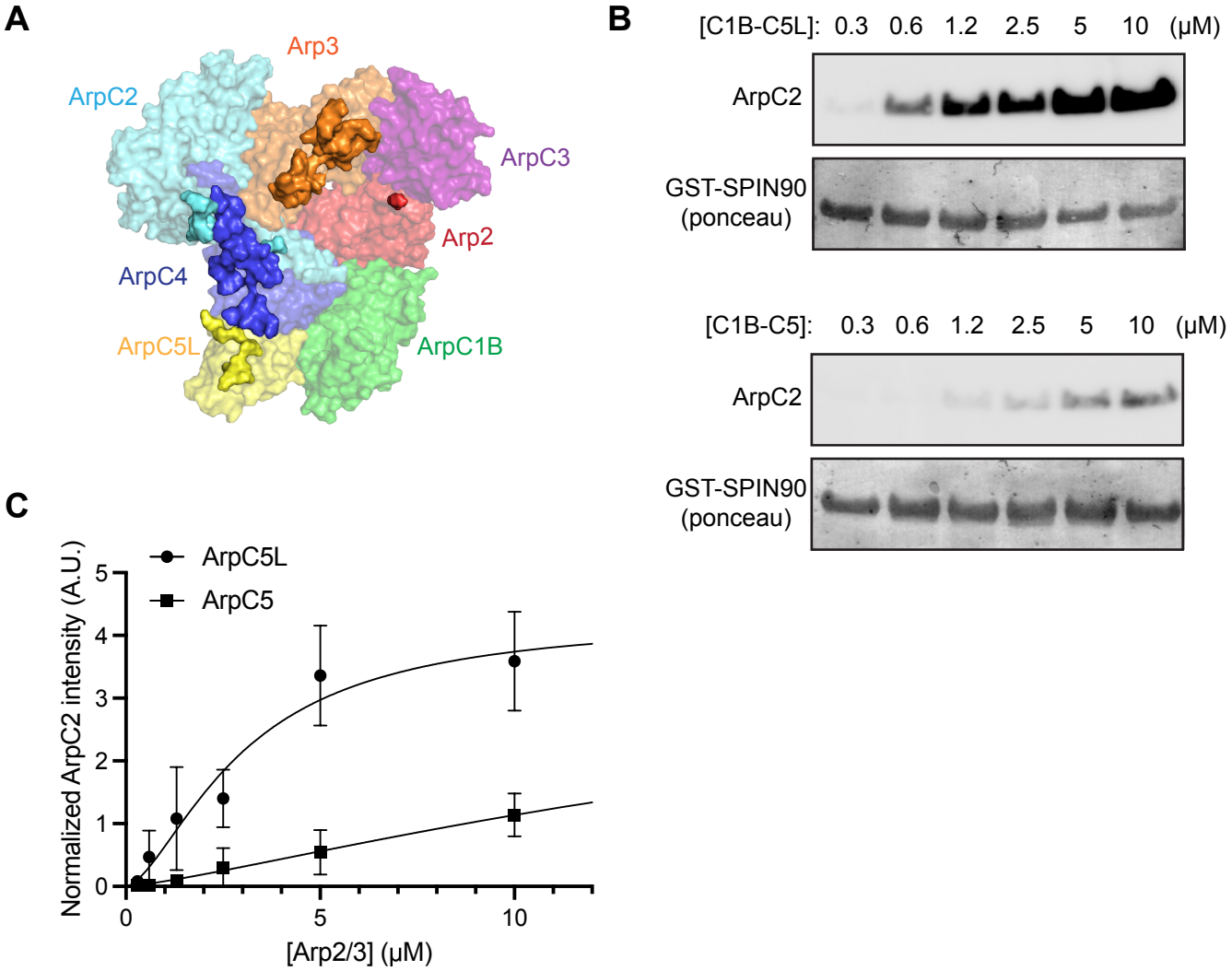
A
Arp3
ArpC2
ArpC3
Arp2
ArpC4
ArpC5L
ArpC1B
B
[C1B-C5L]: 0.3 0.6 1.2 2.5 5 10 (μM)
ArpC2
GST-SPIN90
(ponceau)
[C1B-C5]: 0.3 0.6 1.2 2.5 5 10 (μM)
ArpC2
GST-SPIN90
(ponceau)
C
ArpC5L
ArpC5
Normalized ArpC2 intensity (A.U.)
0
1
2
3
4
5
0
5
10
[Arp2/3] (μM)

Figure 2

A

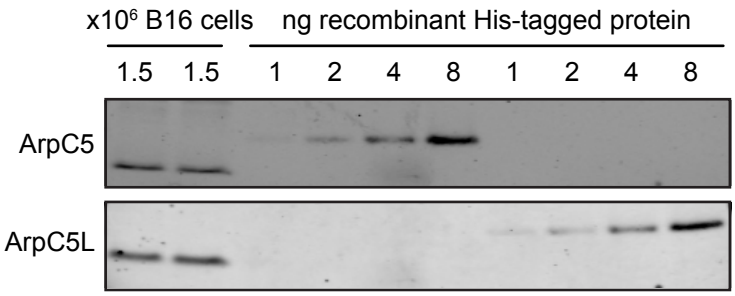

	ArpC5	ArpC5L
nmol/cell ± SD	1.25×10^{-6} 2.0×10^{-7}	2.1×10^{-6} 5.6×10^{-7}

B

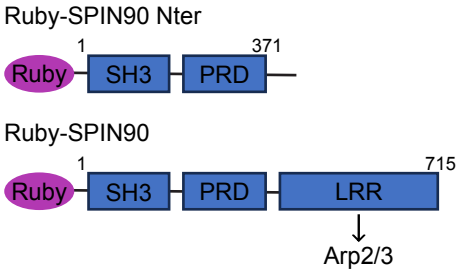

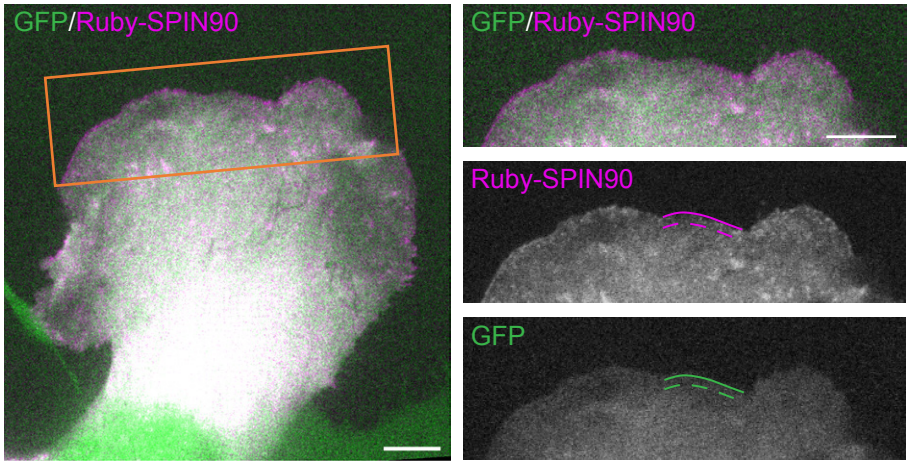

Scale bar = 5 µm

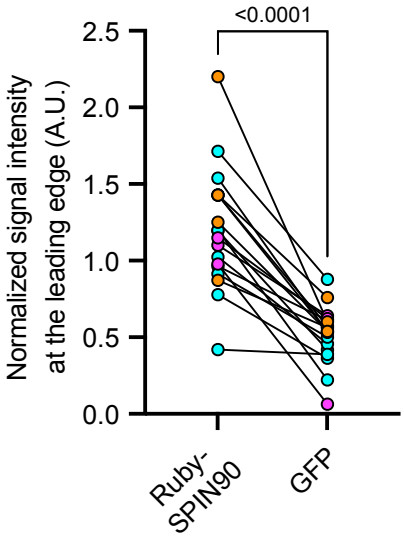

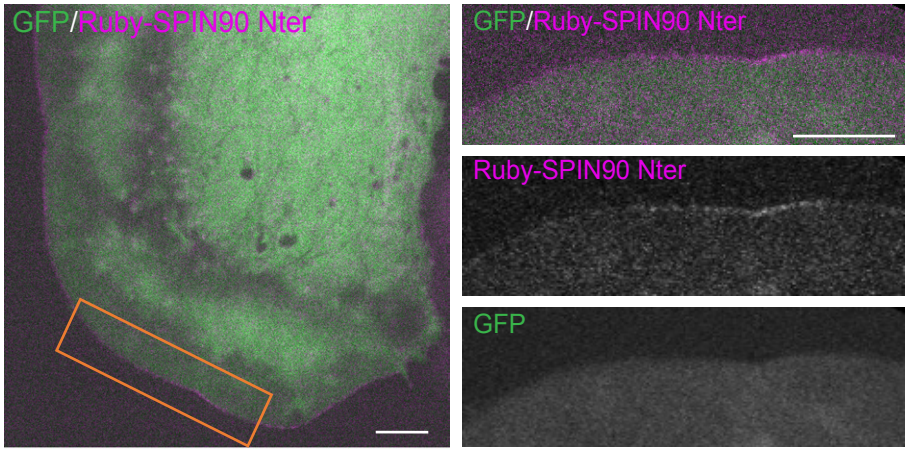

Scale bar = 5 µm

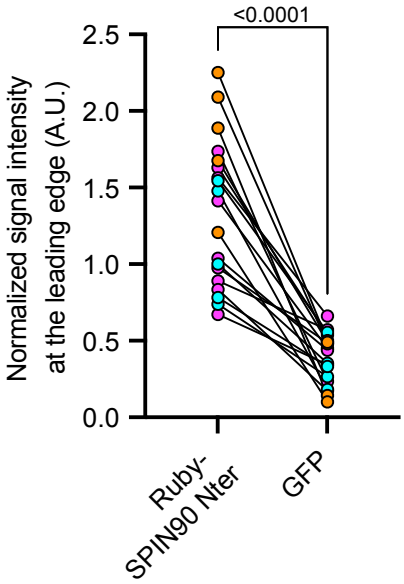

Figure 3

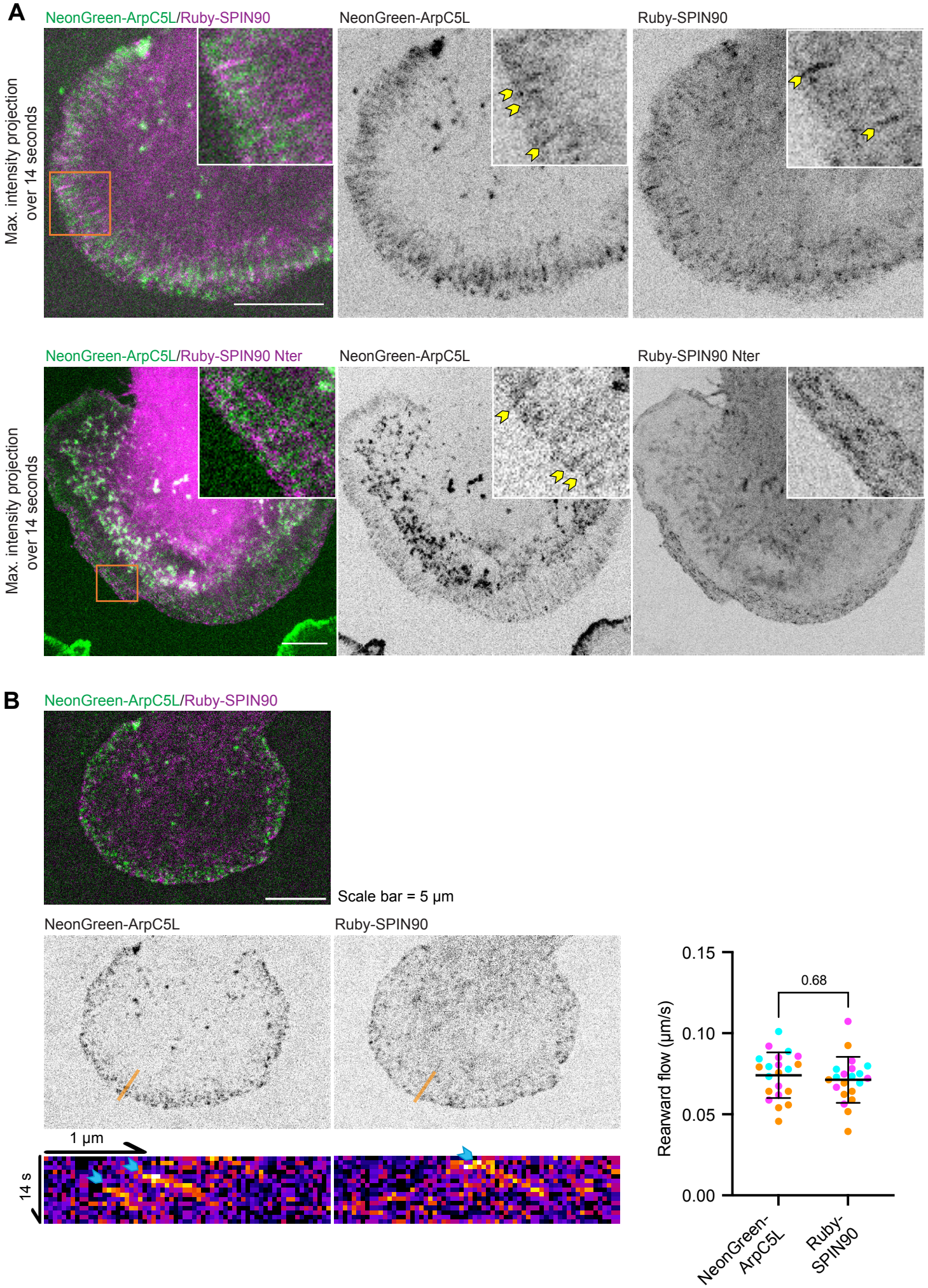
A
NeonGreen-ArpC5L/Ruby-SPIN90
NeonGreen-ArpC5L
Ruby-SPIN90
Max. intensity projection over 14 seconds
NeonGreen-ArpC5L/Ruby-SPIN90 Nter
NeonGreen-ArpC5L
Ruby-SPIN90 Nter
Max. intensity projection over 14 seconds
B
NeonGreen-ArpC5L/Ruby-SPIN90
Scale bar = 5 µm
NeonGreen-ArpC5L
Ruby-SPIN90
1 µm
14 s
Rearward flow (µm/s)
0.15
0.10
0.05
0.00
0.68
NeonGreen-ArpC5L
Ruby-SPIN90

Figure 4

A

NeonGreen-ArpC5L

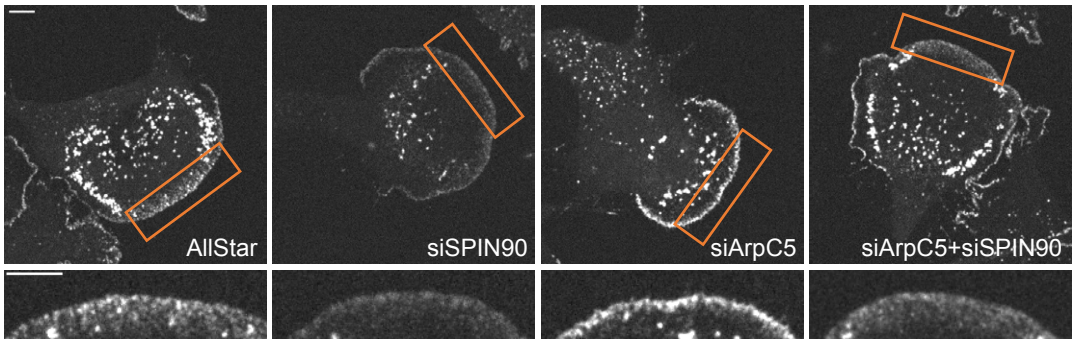

Scale bar = 5 μm

ArpC5L signal at the leading edge

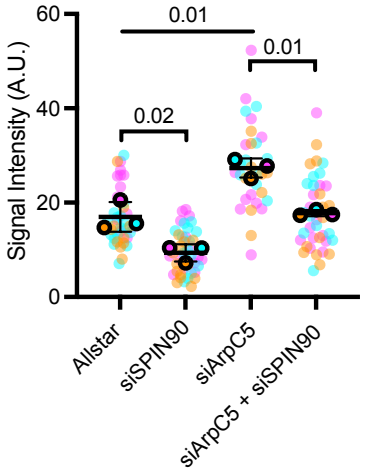

B

ArpC5-NeonGreen

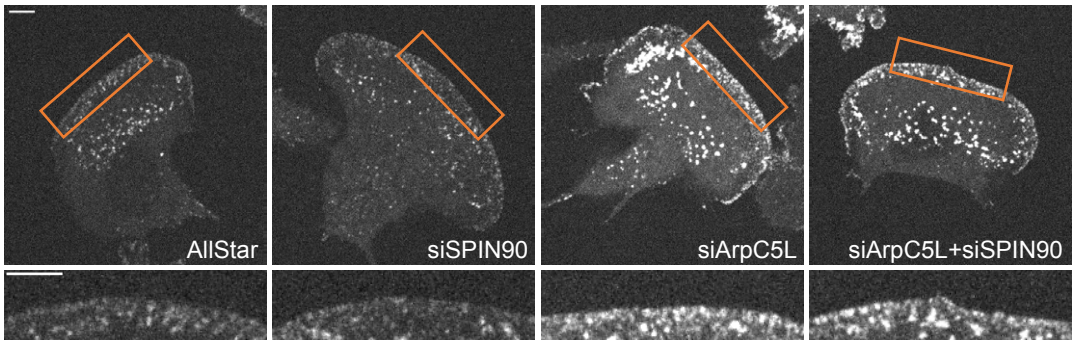

Scale bar = 5 μm

ArpC5 signal at the leading edge

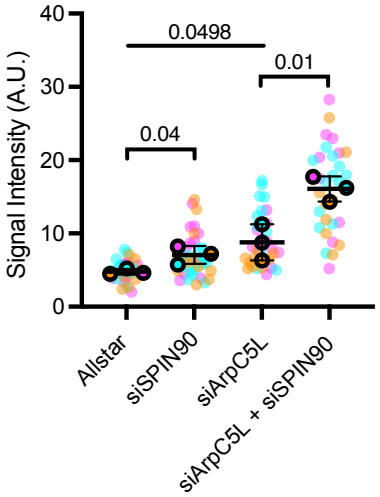

Figure 5

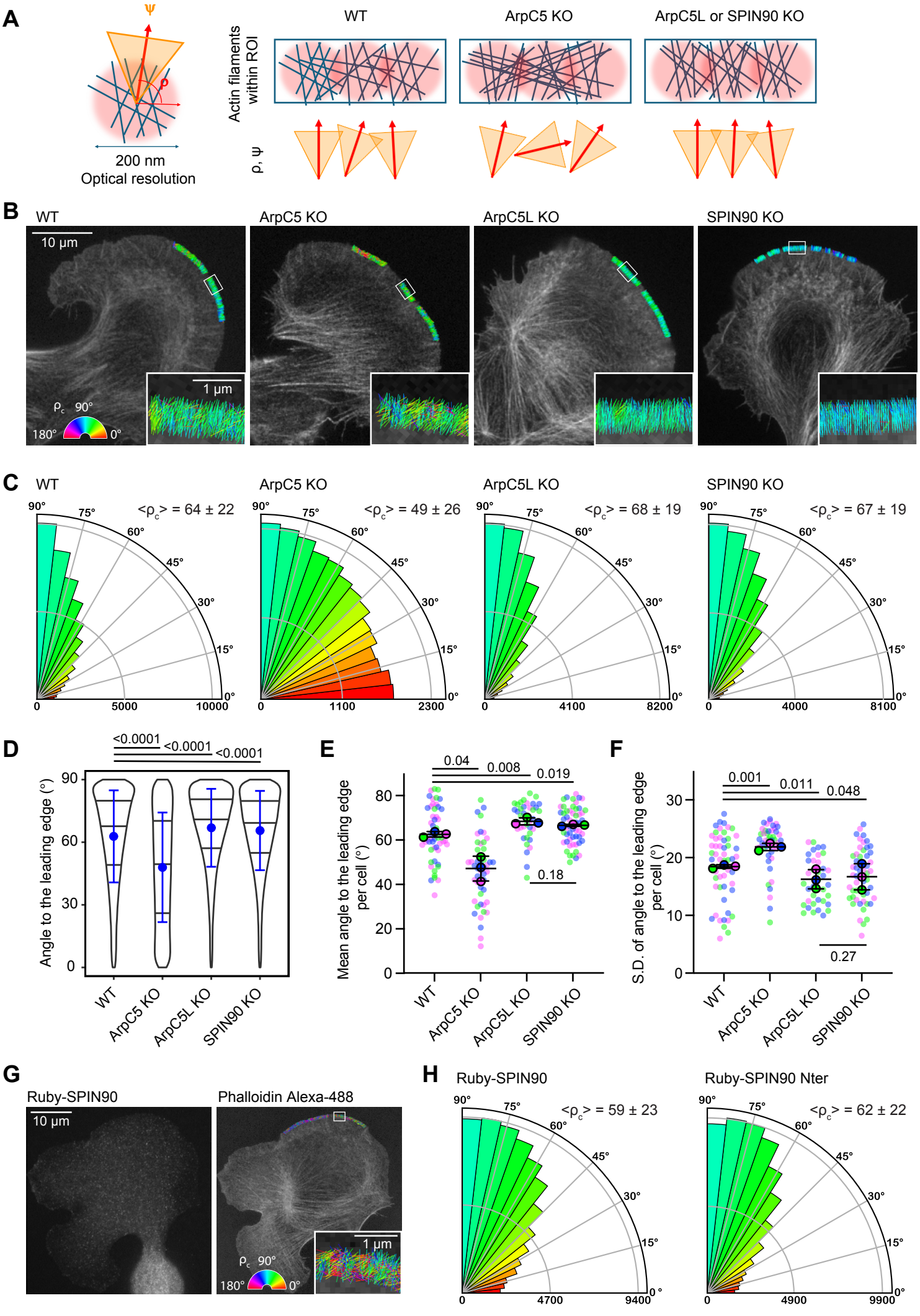
A
ψ
ρ
200 nm
Optical resolution
WT
ArpC5 KO
ArpC5L or SPIN90 KO
Actin filaments within ROI
ρ, ψ
B
WT
ArpC5 KO
ArpC5L KO
SPIN90 KO
10 µm
1 µm
ρc 90°
180°
0°
C
WT
ArpC5 KO
ArpC5L KO
SPIN90 KO
<ρc> = 64 ± 22
<ρc> = 49 ± 26
<ρc> = 68 ± 19
<ρc> = 67 ± 19
90°
75°
60°
45°
30°
15°
0°
0
5000
10000
1100
2300
4100
8200
4000
8100
D
<0.0001
<0.0001
<0.0001
Angle to the leading edge (°)
90
60
30
0
WT
ArpC5 KO
ArpC5L KO
SPIN90 KO
E
0.04
0.008
0.019
0.18
Mean angle to the leading edge per cell (°)
80
60
40
20
0
WT
ArpC5 KO
ArpC5L KO
SPIN90 KO
F
0.001
0.011
0.048
0.27
S.D. of angle to the leading edge per cell (°)
30
20
10
0
WT
ArpC5 KO
ArpC5L KO
SPIN90 KO
G
Ruby-SPIN90
Phalloidin Alexa-488
10 µm
1 µm
ρc 90°
180°
0°
H
Ruby-SPIN90
Ruby-SPIN90 Nter
<ρc> = 59 ± 23
<ρc> = 62 ± 22
90°
75°
60°
45°
30°
15°
0°
0
4700
9400
4900
9900

Figure 6

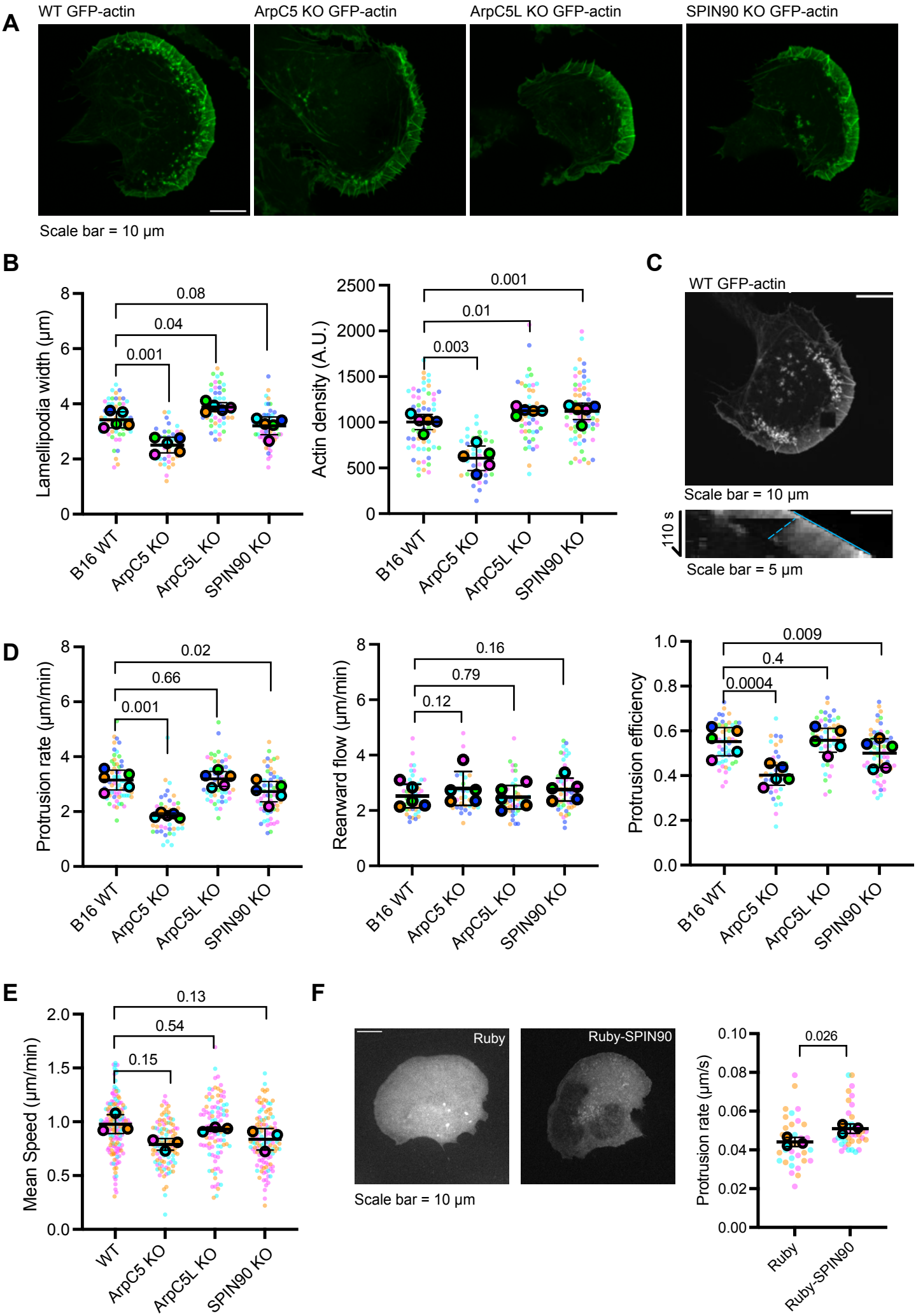
A
WT GFP-actin
ArpC5 KO GFP-actin
ArpC5L KO GFP-actin
SPIN90 KO GFP-actin
Scale bar = 10 µm
B
Lamellipodia width (µm)
0.08
0.04
0.001
Actin density (A.U.)
0.001
0.01
0.003
B16 WT
ArpC5 KO
ArpC5L KO
SPIN90 KO
C
WT GFP-actin
Scale bar = 10 µm
110 s
Scale bar = 5 µm
D
Protrusion rate (µm/min)
0.02
0.66
0.001
Rearward flow (µm/min)
0.16
0.79
0.12
Protrusion efficiency
0.009
0.4
0.0004
E
Mean Speed (µm/min)
0.13
0.54
0.15
WT
F
Ruby
Ruby-SPIN90
Scale bar = 10 µm
Protrusion rate (µm/s)
0.026
Ruby
Ruby-SPIN90

Figure 7

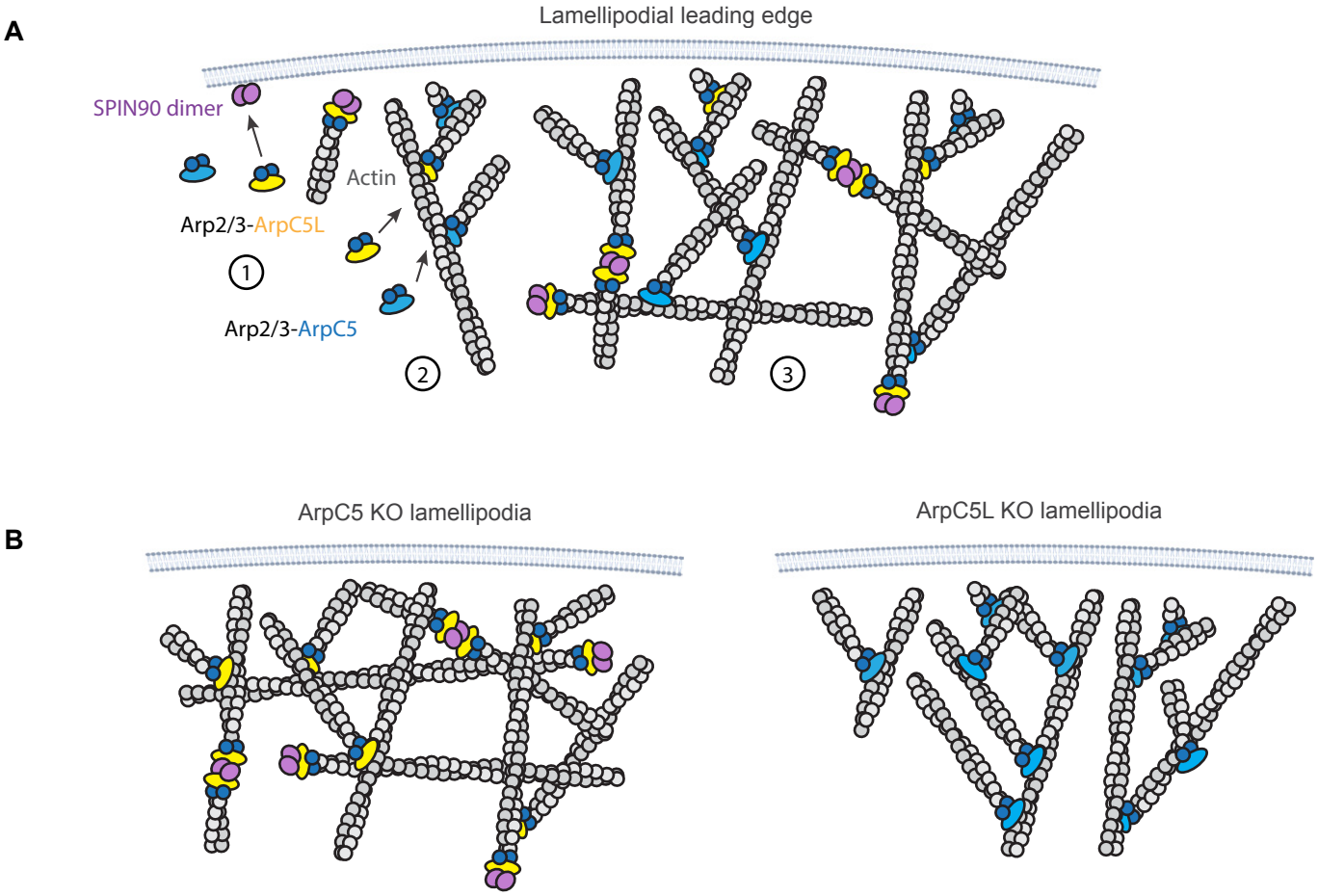
A
Lamellipodial leading edge
SPIN90 dimer
Actin
Arp2/3-ArpC5L
1
Arp2/3-ArpC5
2
3
B
ArpC5 KO lamellipodia
ArpC5L KO lamellipodia

Figure 8